

# Novel Lattice Thermal Transport in Stanene

Bo Peng<sup>1</sup>, Hao Zhang<sup>1,\*</sup>, Hezhu Shao<sup>2</sup>, Yuchen Xu<sup>1</sup>, Xiangchao Zhang<sup>1</sup> and Heyuan Zhu<sup>1</sup>

<sup>1</sup>*Shanghai Ultra-precision Optical Manufacturing Engineering Center,  
Department of Optical Science and Engineering, Fudan University, Shanghai 200433, China and*

<sup>2</sup>*Ningbo Institute of Materials Technology and Engineering,  
Chinese Academy of Science, Ningbo 315201, China\**

A fundamental understanding of phonon transport in stanene is crucial to predict the thermal performance of its potential devices. Using first principle calculations, we predict the lattice thermal conductivity of stanene. Strong anisotropy in thermal conductivity is observed. The acoustical and optical contributions to the lattice thermal conductivity are evaluated. Detailed analysis of phase space for three-phonon processes shows that phonon scattering channels  $ZA \rightarrow LA/TA/ZA + LA/TA/ZA$  are severely restricted, leading to the dominant contributions of ZA phonons to the thermal conductivity. The size dependence of thermal conductivity is investigated as well for the purpose of the design of thermoelectric nanostructures.

## I. INTRODUCTION

Research in 2D materials has experienced an explosion of interest due to their potential for integration into next-generation electronic and energy conversion devices<sup>1–4</sup>. Recently, a new 2D material, stanene, has been realized on the  $\text{Bi}_2\text{Te}_3(111)$  substrate by molecular beam epitaxy<sup>5</sup>, and attracted tremendous interest due to its outstanding properties. For instance, stanene could provide topological superconductivity, which allows the film to conduct electricity without losing energy as waste heat<sup>6</sup>. Moreover, stanene has enhanced thermoelectric (TE) performance due to its strongly size-dependent TE properties, which can open new directions for the science and technology of thermoelectrics<sup>7</sup>.

Stanene, a monolayer of tin film with buckled honeycomb structure like silicene, is predicted to be an example of a topological insulator<sup>5,6</sup>. It has been reported that a nontrivial bulk gap of 0.1 eV opens when the spin-orbital coupling is present in stanene, and the edge states are gapless with bands dispersing inside the bulk gap and helical with spin-momentum locking, which can be used as dissipationless conducting “wires” for electronic circuits<sup>6</sup>. In addition, recent study has found that the thermoelectric figure of merit  $zT$  is strongly size dependent in stanene, and can be improved to be significantly larger than 1 by optimizing the geometric size<sup>7</sup>. All these electrical and thermoelectrical applications of stanene are closely related to its thermal properties. For instance, high TE performance requires a low thermal conductivity, which consists of electronic thermal conductivity and lattice thermal conductivity<sup>8</sup>. However, the lattice thermal conductivity of stanene has not been investigated in detail. Furthermore, although the size dependence of  $zT$  and the Seebeck coefficient in stanene has been studied for the purpose of thermoelectrical applications, the size dependence of lattice thermal conductivity, which is also crucial when designing TE-application nanostructures<sup>9</sup>, remains uninvestigated.

In this paper, we calculate the lattice thermal conductivity  $\kappa$  of stanene using an iterative solution of the Boltzmann transport equation (BTE) for phonons<sup>10</sup>. We find that the in-plane lattice thermal transport in stanene is strongly anisotropic, and the  $\kappa$  along the zigzag direction is nearly twice the  $\kappa$  along the armchair direction. While the strong anisotropy in lattice thermal conductivity is observed only in hinge-like structures such as black phosphorene and  $\text{SnSe}$ <sup>11–13</sup>, no other 2D hexagonal materials with buckled structure show the in-plane anisotropy as we predict for stanene herein. We also extract the contribution of each phonon mode to investigate the underlying mechanism behind the novel thermal transport properties in stanene, and find ZA phonons contribute most to the thermal conductivity (>90%) over a wide temperature range, which is due to their severely restricted phase space for emission processes. Finally, we obtain the representative mean free path (MFP) of stanene that is useful when designing TE nanostructures.

## II. RESULTS

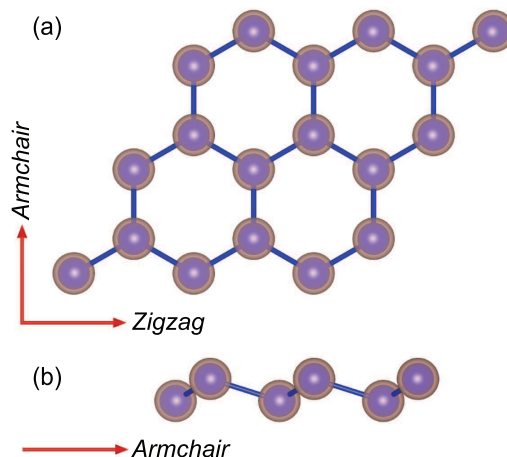


FIG. 1. (a)Top view and (b)side view of stanene. The zigzag and armchair directions are indicated with red arrows.

Fig. 1 shows the optimized structure of stanene with vectors indicating zigzag and armchair directions, respectively. A similar low-buckled configuration is also found in silicene and blue phosphorene<sup>11,14</sup>, which is different from the

planar geometry of graphene<sup>15</sup>. The optimized lattice constant is 4.67 Å, which is in good agreement with the previous work<sup>6</sup>. There are two tin atoms in one unit cell, corresponding to three acoustic and three optical phonon branches.

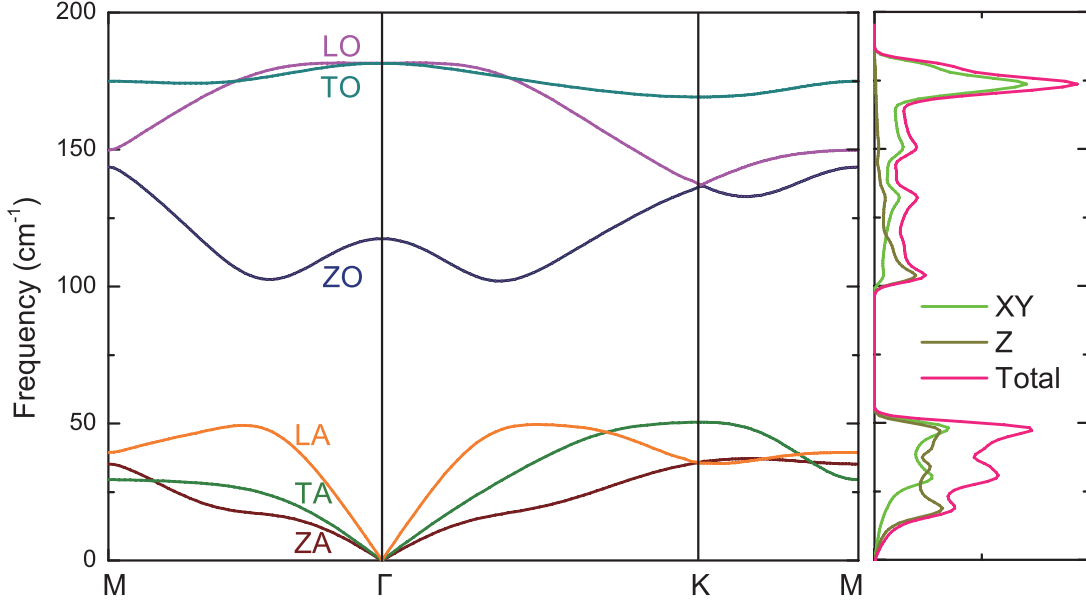


FIG. 2. Phonon dispersion and DOS of stanene. Three acoustic and three optical phonon modes are indicated with different colors.

Fig. 2 shows the calculated phonon dispersion. Similar to  $\alpha$ -Sn and  $\beta$ -Sn<sup>16</sup>, the longitudinal acoustic (LA), transverse acoustic (TA), and z-direction acoustic (ZA) branches of stanene are linear near the  $\Gamma$  point, which is distinctly different from the quadratic ZA-branch dispersion in the typical 2D materials<sup>12,17–19</sup>. Using the phonon spectrum, we calculate the group velocities of acoustic phonons along  $\Gamma$ -M and  $\Gamma$ -K respectively, as shown in Fig. 3. The anisotropy in group velocities along the two directions is similar to that of phosphorene and SnSe<sup>12,13</sup>. The Debye temperature  $\Theta_D$  can be calculated with the highest frequency of normal mode vibration (Debye frequency)  $\nu_m = 1.51$  THz,

$$\Theta_D = h\nu_m/k_B \quad (1)$$

where  $h$  is the Planck constant, and  $k_B$  is the Boltzmann constant. The calculated Debye temperature is 72.5 K, which is nearly three times smaller than the previous value of  $\beta$ -Sn of  $200 \pm 3$  K<sup>20</sup>.

The intrinsic lattice thermal conductivity  $\kappa$  of naturally occurring stanene is shown in Fig. 4. The  $\kappa$  along the zigzag direction is almost twice the  $\kappa$  along the armchair direction, which shows obvious anisotropic properties. Similar anisotropy of thermal conductivity is found in black phosphorene and SnSe<sup>12,13</sup>, which possess the hinge-like structure, in contrast to the isotropic  $\kappa$  observed in other 2D hexagonal materials such as silicene, blue phosphorene, graphene, and monolayer MoS<sub>2</sub><sup>11,19,21,22</sup>. The anisotropy may be due to the asymmetry of group velocities along  $\Gamma$ -M (zigzag) and  $\Gamma$ -K (armchair) directions. It should be noted that, to the best of our knowledge, no other 2D hexagonal materials show the in-plane anisotropy as we observed in stanene.

The thermal conductivity at 300 K is  $5.40 \text{ W m}^{-1} \text{ K}^{-1}$  (zigzag) and  $3.07 \text{ W m}^{-1} \text{ K}^{-1}$  (armchair) for naturally occurring stanene,  $5.41 \text{ W m}^{-1} \text{ K}^{-1}$  (zigzag) and  $3.08 \text{ W m}^{-1} \text{ K}^{-1}$  (armchair) for isotopically pure stanene, respectively. The measured room-temperature  $\kappa$  of 500 nm tin film is  $46 \pm 4.2 \text{ W m}^{-1} \text{ K}^{-1}$  while for the 100 nm tin film the  $\kappa$  is  $36 \pm 2.88 \text{ W m}^{-1} \text{ K}^{-1}$ <sup>23</sup>, which are lower than the room-temperature value of  $\kappa$  of bulk tin,  $64 \text{ W m}^{-1} \text{ K}^{-1}$ . Note that when the thickness of the Sn thin film decreases, phonons exhibit boundary scattering more significantly<sup>23</sup>, which further reduces the value of  $\kappa$ . Thus the small calculated value of  $\kappa$  in stanene is reasonable.

Furthermore, we fit the calculated  $\kappa$  along armchair and zigzag directions respectively, with an inverse relation to temperature, i.e.  $\kappa \sim 1/T$ . As shown in Fig. 4, the fitted  $\kappa$  plotted as dot lines coincides perfectly with the calculated  $\kappa$ . According to the kinetic formula for the thermal conductivity of an assembly of total specific heat  $C$ , average phonon velocity  $v$ , and mean free path (MFP)  $l$ , i.e.  $\kappa = Cvl$ , when the temperature is well above the Debye temperature  $\Theta_D$ , the  $C$  is constant, while the dominant three-phonon anharmonic processes at high temperatures lead to  $l \propto 1/T$ <sup>24,25</sup>. Such inverse relationship of  $\kappa$  and  $T$  is also found in other materials such as graphene, black phosphorene, PbSe, and Mg<sub>2</sub>(Si,Sn) when  $T > \Theta_D$ <sup>12,26–28</sup>.

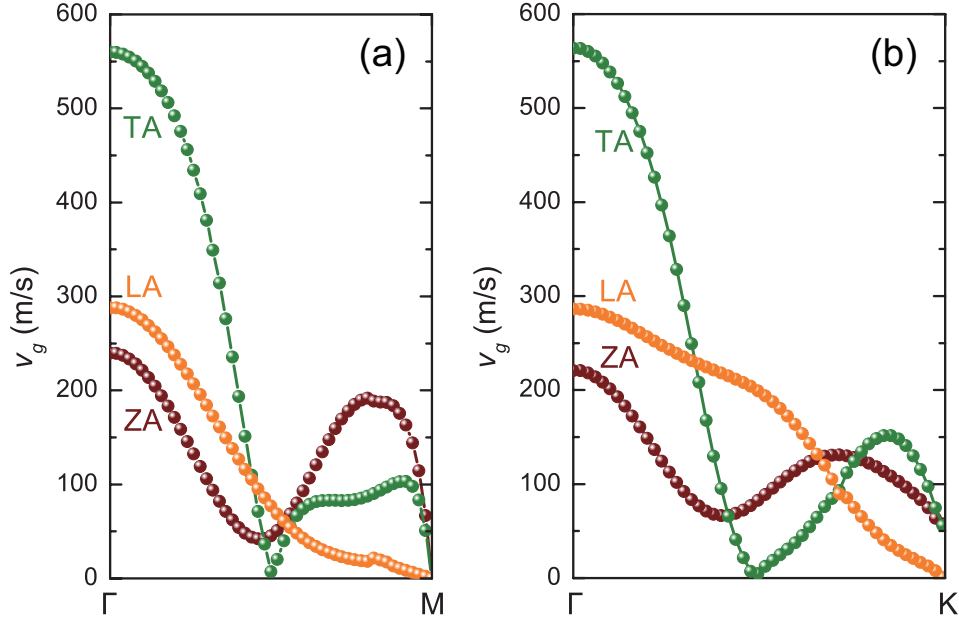


FIG. 3. Phonon group velocities along the (a) $\Gamma$ -M and (b) $\Gamma$ -K direction.

Compared to other 2D hexagonal materials, the  $\kappa$  of stanene is smaller than that of silicene ( $9.4 \text{ W m}^{-1} \text{ K}^{-1}$ - $26 \text{ W m}^{-1} \text{ K}^{-1}$ )<sup>19,29</sup>, one to two orders of magnitude larger than those of monolayer MoS<sub>2</sub> ( $110 \pm 20 \text{ W m}^{-1} \text{ K}^{-1}$ )<sup>30</sup> and blue phosphorene ( $78 \text{ W m}^{-1} \text{ K}^{-1}$ )<sup>11</sup>, while at least three orders of magnitude lower than that of graphene ( $3000 \text{ W m}^{-1} \text{ K}^{-1}$ )<sup>19</sup>. The lower  $\kappa$  of stanene is due to its smaller sound velocities (200-600 m/s compared to 5,400-8,800 m/s in silicene<sup>31</sup>, 700-1,100 m/s in MoS<sub>2</sub><sup>32</sup>, 4,000-8,000 m/s in blue phosphorene<sup>11</sup>, and 3,700-6,000 m/s in graphene<sup>33</sup>), and lower Debye temperatures (72.5 K compared to 500 K for monolayer MoS<sub>2</sub> and blue phosphorene<sup>11,34</sup>, and 2,300 K for graphene<sup>35</sup>) which results in higher phonon scattering rates since more phonon modes are active at a given temperature.

In order to understand the fundamental mechanism of phonon transport in stanene, we examine the contributions of different phonon branches to  $\kappa$  of stanene along both zigzag and armchair directions, as shown in Fig. 5. The contribution of the ZA phonons is around 93% and 91% at temperatures ranging from 100 K to 800 K for zigzag and armchair directions respectively. The contribution of ZA phonons to the  $\kappa$  of stanene is close to that of graphene (80%)<sup>19</sup> but larger than that of blue phosphorene (44%)<sup>11</sup> and monolayer MoS<sub>2</sub> (39%)<sup>22</sup>, while much larger than that of silicene (7.5%)<sup>19</sup>. It has been reported that the large contribution of the ZA mode to the  $\kappa$  of graphene is due to a symmetry selection rule in one-atom-thick materials, which strongly restricts anharmonic phonon-phonon scattering of the ZA mode<sup>26</sup>, while the buckled structure in silicene and blue phosphorene breaks out the out-of-plane symmetry, in which the selection rule does not apply. As a result, the predicted contribution of ZA phonons to  $\kappa$  in silicene and blue phosphorene much smaller than in graphene at 300 K. However, it is surprisingly found herein that the contribution of ZA phonons in buckled stanene is even larger than in graphene.

Considering the significant difference in the contribution of the ZA modes to the  $\kappa$  in stanene and other 2D hexagonal materials, it is worthwhile to investigate the relaxation time of each phonon mode as a function of frequency, as shown in Fig. 6. In Fig. 6(a), the three-phonon relaxation time of ZA mode and TA mode is much longer than that of LA mode, and the relaxation time of the optical phonons is much shorter than the acoustic phonons. We also calculate the isotopic relaxation time, as shown in the inset of Fig. 6(a). Isotopic scattering processes are wavelength-dependent. The long-wavelength phonons can transport all the heat with very little isotopic scattering<sup>36</sup>, thus we observe the relative long relaxation time of acoustic phonons at low frequencies. The inverse of total relaxation time is a sum of contributions from anharmonic scattering and isotopic scattering,

$$1/\tau_{\lambda} = 1/\tau_{\lambda}^{anh} + 1/\tau_{\lambda}^{iso} \quad (2)$$

where  $\lambda$  comprises both a phonon branch index  $j$  and a wave vector  $\mathbf{q}$ . Thus the three-phonon processes with much shorter relaxation time dominate the behaviour of the lattice thermal conductivity. The total relaxation time is shown in Fig. 6(b). The total relaxation time in stanene is at least one order of magnitude smaller than other 2D hexagonal materials such as graphene, MoS<sub>2</sub>, and silicene<sup>31,37,38</sup>. Although the relaxation time of ZA mode is the longest among

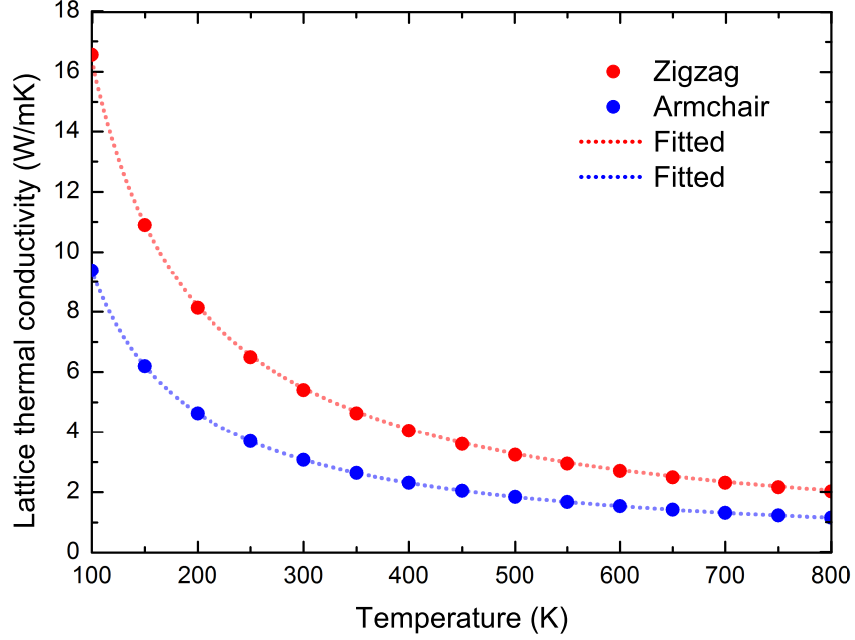


FIG. 4. Calculated lattice thermal conductivity  $\kappa$  of stanene along zigzag (red) and armchair (blue) directions as a function of temperature ranging from 100 K to 800 K. The inverse relationship of  $\kappa$  and temperature ( $\kappa \sim 1/T$ ) is displayed as dot lines.

the three acoustic branches, it is comparable to that of other acoustic phonon modes. Consequently, the dominant contribution from ZA branch to  $\kappa$  in buckled stanene can not be understood clearly by only considering the relaxation time.

To understand the effect of the selection rule, the key physical insight can be obtained by calculating the phase space for three-phonon processes ( $P_3$ ) in the temperature range where these processes are dominant,

$$P_3 = \frac{2}{3\Omega}(P_3^{(+)} + \frac{1}{2}P_3^{(-)}) \quad (3)$$

where  $\Omega$  is a normalization factor, and

$$P_3^{(\pm)} = \sum_j \int d\mathbf{q} D_j^{(\pm)}(\mathbf{q}) \quad (4)$$

and

$$D_j^{(\pm)}(\mathbf{q}) = \sum_{j', j''} \int d\mathbf{q}' \delta(\omega_j(\mathbf{q}) \pm \omega_{j'}(\mathbf{q}') - \omega_{j''}(\mathbf{q} \pm \mathbf{q}' - \mathbf{G})) \quad (5)$$

where  $D_j^{(+)}(\mathbf{q})$  corresponds to absorption processes, i.e.  $\omega_j(\mathbf{q}) + \omega_{j'}(\mathbf{q}') = \omega_{j''}(\mathbf{q} \pm \mathbf{q}' - \mathbf{G})$ , whereas  $D_j^{(-)}(\mathbf{q})$  corresponds to emission processes, i.e.  $\omega_j(\mathbf{q}) = \omega_{j'}(\mathbf{q}') + \omega_{j''}(\mathbf{q} \pm \mathbf{q}' - \mathbf{G})$ . According to Eq. 3, the phase space  $P_3$  can be used to assess the quantity of phonon modes available for absorption and emission processes, and the results are shown in Fig. 7. It has been confirmed that there is an inverse relationship between phase space for three-phonon processes and the intrinsic lattice thermal conductivity for a material<sup>24,39</sup>.

The selection rule in graphene that arises from the reflection symmetry perpendicular to the graphene plane restricts the participation of odd number of ZA phonons in three-phonon processes, e.g.  $\text{ZA} + \text{ZA} \leftrightarrow \text{ZA}$ ,  $\text{ZA} + \text{LA}/\text{TA} \leftrightarrow \text{LA}/\text{TA}$ . As a result, 60% of the phase space of ZA phonons is forbidden by such selection rule, which leads to the dominant

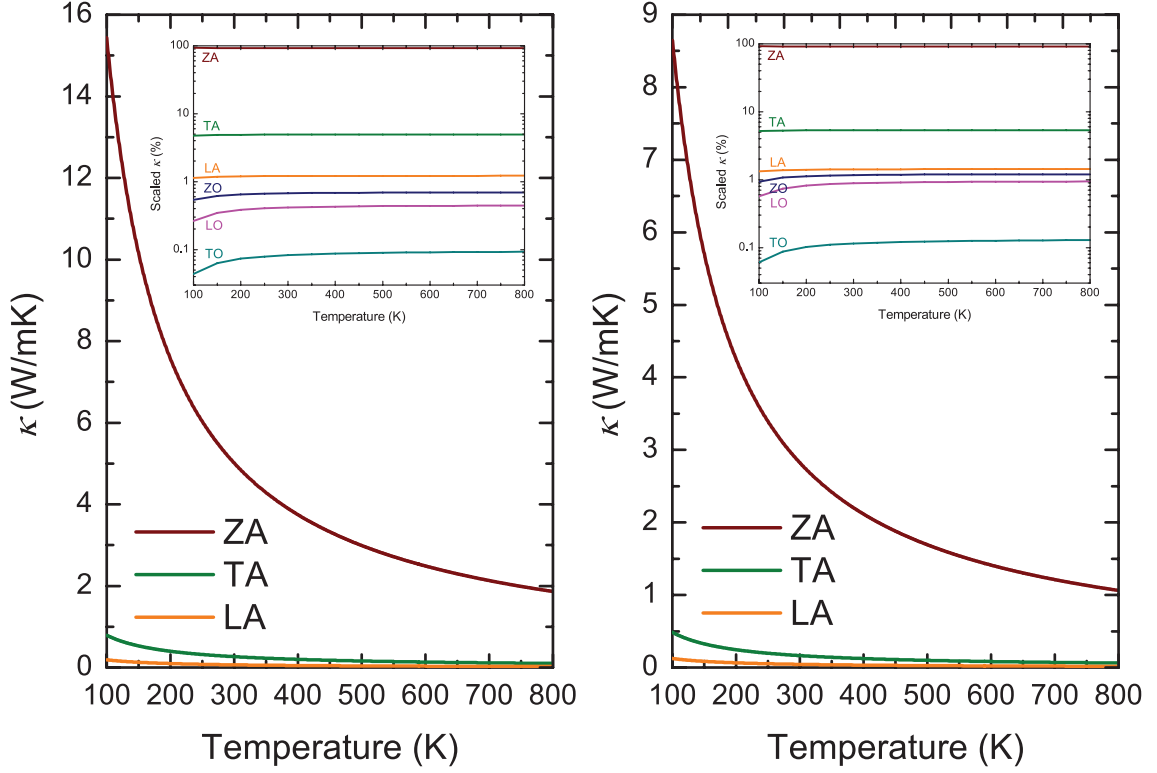


FIG. 5. The temperature dependence on thermal conductivity of LA, TA, and ZA modes along (a) zigzag and (b) armchair directions. Percentage contribution of each phonon mode to  $\kappa$  is shown in the insets.

contribution of the ZA mode to  $\kappa$  in graphene. For the buckled stanene where the reflection-symmetry selection rule does not apply, the phase space  $P_3$  of ZA phonons available for both absorption and emission processes is not reduced consequently. It is shown in Fig. 7(a) that the phase space for absorption processes  $P_3^{(+)}$  of ZA phonons is relatively large, which subsequently leads to a less contribution to  $\kappa$ . However, the phase space for emission processes  $P_3^{(-)}$  of ZA phonons has much smaller values in Fig. 7(b), which enables the emission processes of ZA modes to be the most significant contribution to  $\kappa$ . Since the energy of ZA phonons at frequencies below  $25 \text{ cm}^{-1}$  are relatively small, the scattering channels,  $\text{ZA} \rightarrow \text{LA}/\text{TA}/\text{ZA} + \text{LA}/\text{TA}/\text{ZA}$ , are severely restricted, and the allowed three-phonon phase space is subsequently reduced, as shown in Fig. 7(b), which leads to the dominant contribution of ZA phonons involved in emission processes to  $\kappa$  in stanene. Therefore, although the symmetry selection rule does not apply in stanene compared to graphene, the restricted phase space for emission processes of ZA phonons due to their relatively small energy, ensures that their dominant contribution to  $\kappa$  will extend over a wide temperature range.

Furthermore, we investigate the size dependence of  $\kappa$  by calculating the cumulative thermal conductivity with respect to the maximum MFP allowed. The cumulative thermal conductivity of stanene for both zigzag and armchair directions at 300 K and 600 K are plotted in Fig. 8(a) and 8(b), respectively. The cumulated  $\kappa$  keeps increasing as MFP increases, until reaching the thermodynamic limit above a length scale  $L_{diff}$  which represents the longest mean free path of the heat carriers. The  $L_{diff}$  at 300 K and 600 K is 1321.4 nm and 656.1 nm, respectively. It is found that phonons with MFPs below 611.7 nm (zigzag) and 587.4 nm (armchair) at 300 K, and below 304.9 nm (zigzag) and 292.7 nm (armchair) at 600 K, contribute around 75% of the total  $\kappa$ , which indicates that the design of nanostructures can be utilized to enhance the thermoelectric figure of merit. In order to properly reduce  $\kappa$  for thermoelectric applications, we can fit the cumulative  $\kappa$  to a uniparametric function<sup>10</sup>

$$\kappa(l \leq l_{max}) = \frac{\kappa_{max}}{1 + \frac{l_0}{l_{max}}}, \quad (6)$$

where  $\kappa_{max}$  is the ultimate cumulative thermal conductivity,  $l_{max}$  is the maximal MFP concerned, and  $l_0$  is the parameter to be evaluated. The fitted curves at 300 K and 600 K are plotted in Fig. 8(a) and 8(b), reproducing both

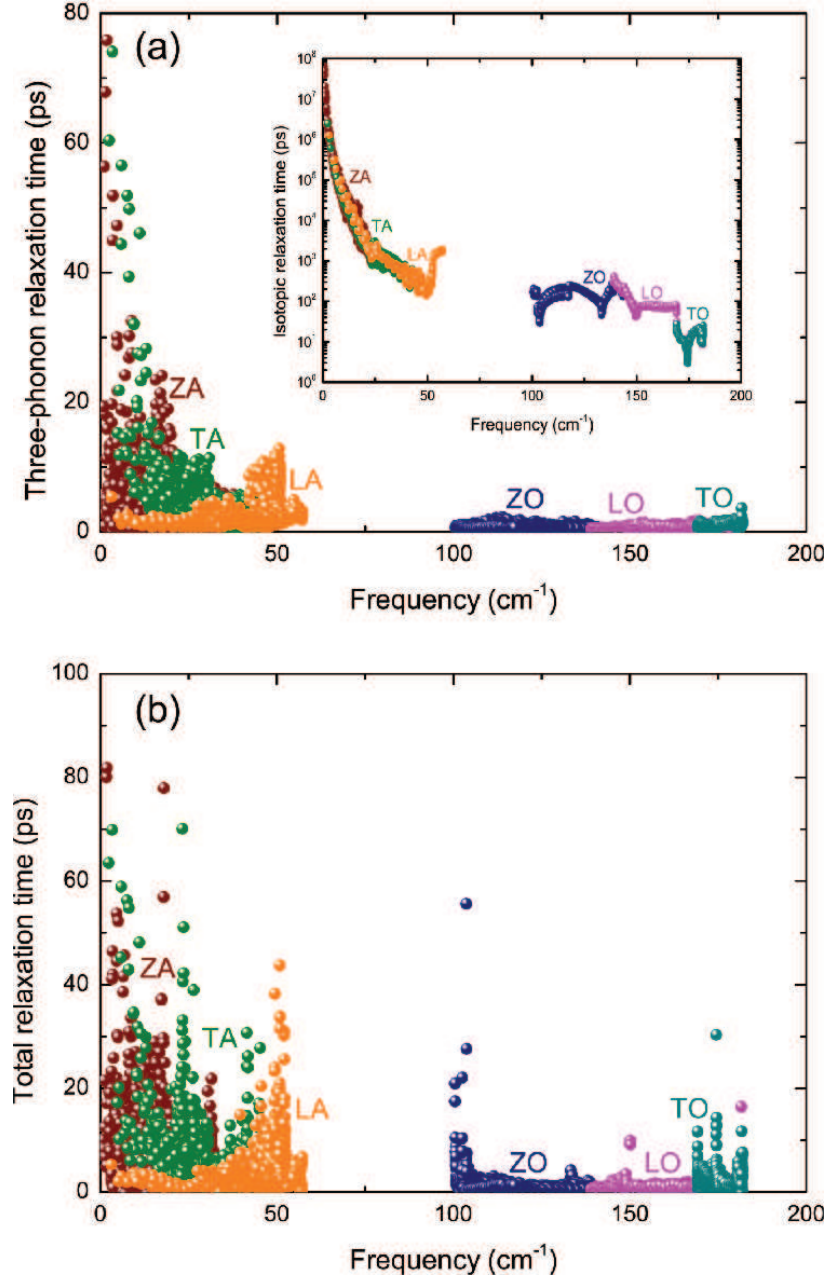


FIG. 6. The (a)three-phonon and (b)total relaxation time of each phonon branch as a function of frequency. The isotopic relaxation time is shown in the inset of (a).

the slope and the position of the calculated data well. It yields the parameter  $l_0$  of 220.2 nm (109.3 nm) and 159.5 nm (79.1 nm) for zigzag and armchair directions at 300 K (600 K), which can be interpreted as representative of the MFP of relevant heat-carrying phonons in stanene.

Furthermore, as the size get smaller, when the nanostructuring induced phonon scattering becomes dominant over the three-phonon scattering, the small-grain-limit reduced  $\kappa$  becomes proportional to a constant value  $l_{SG}$ <sup>10</sup>. We calculate the ratio of the thermal conductivity to the thermal conductivity per unit of MFP in the small-grain limit; for stanene the  $l_{SG}$  is found to be 29.1 nm (zigzag) and 19.1 nm (armchair) at 300 K, and 14.4 nm (zigzag) and 9.4 nm (armchair) at 600 K. This quantity is crucial for the thermal design to modulate the thermal conductivity in the small-grain limit.



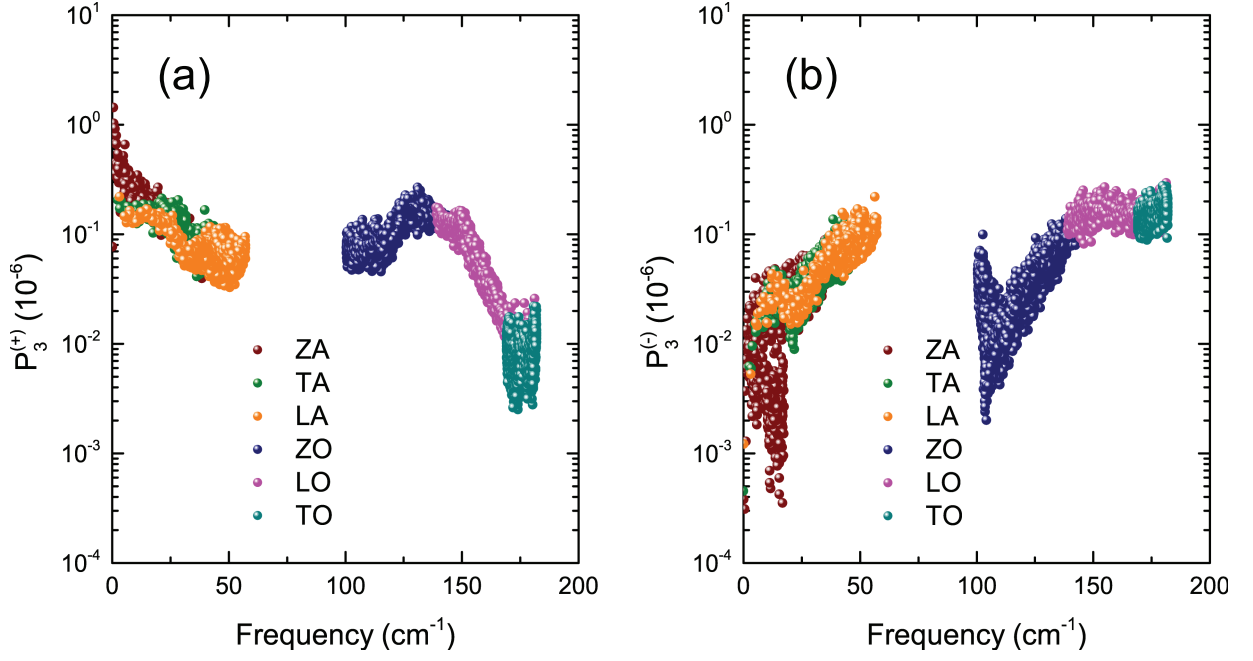


FIG. 7. Frequency-dependence of three-phonon scattering phase space at 300 K for (a) absorption processes and (b) emission processes.

### III. SUMMARY

We predict the lattice thermal conductivity of stanene using first principle calculations and an iterative solution of the BTE. Strong anisotropy is found in the thermal conductivity of stanene. The predicted contribution of ZA phonons to thermal conductivity in stanene is larger than 90% due to their restricted phase space for emission processes. The predicted thermal conductivity of stanene along both zigzag and armchair directions is much smaller than other 2D materials. The representative MFP of stanene is obtained for the purpose of future design in TE-application nanostructures.

### ACKNOWLEDGEMENT

This work is supported by the National Natural Science Foundation of China under Grant No. 11374063.

### IV. METHODS

All the calculations are performed using the Vienna *ab-initio* simulation package (VASP) based on density functional theory (DFT)<sup>40</sup>. We choose the generalized gradient approximation (GGA) in the Perdew-Burke-Ernzerhof (PBE) parametrization for the exchange-correlation functional. We use the projector-augmented-wave potential with 4*d* electrons of tin described as valence, and a plane-wave basis set is employed with kinetic energy cutoff of 500 eV. A 15×15×1 **k**-mesh is used during structural relaxation for the unit cell until the energy differences are converged within 10<sup>-6</sup> eV, with a Hellman-Feynman force convergence threshold of 10<sup>-4</sup> eV/Å. We maintain the interlayer vacuum spacing larger than 15 Å to eliminate the interaction with periodic boundary condition.

In the calculation of phonon dispersion, the harmonic interatomic force constants (IFCs) are obtained using density functional perturbation theory (DFPT), which calculates the dynamical matrix through the linear response of electron density<sup>41</sup>. The 5×5×1 supercell with 5×5×1 **k**-mesh is used to ensure the convergence. The phonon dispersion is obtained using the Phonopy code with the harmonic IFCs as input<sup>42</sup>.

To calculate thermal conductivity of stanene, anharmonic third order IFCs are needed, besides the harmonic IFCs mentioned above. The same 5×5×1 supercell and 5×5×1 **k**-mesh are used to obtain the anharmonic IFCs, and an interaction range of 5.5 Å is considered herein. We calculate the thermal conductivity of naturally occurring and



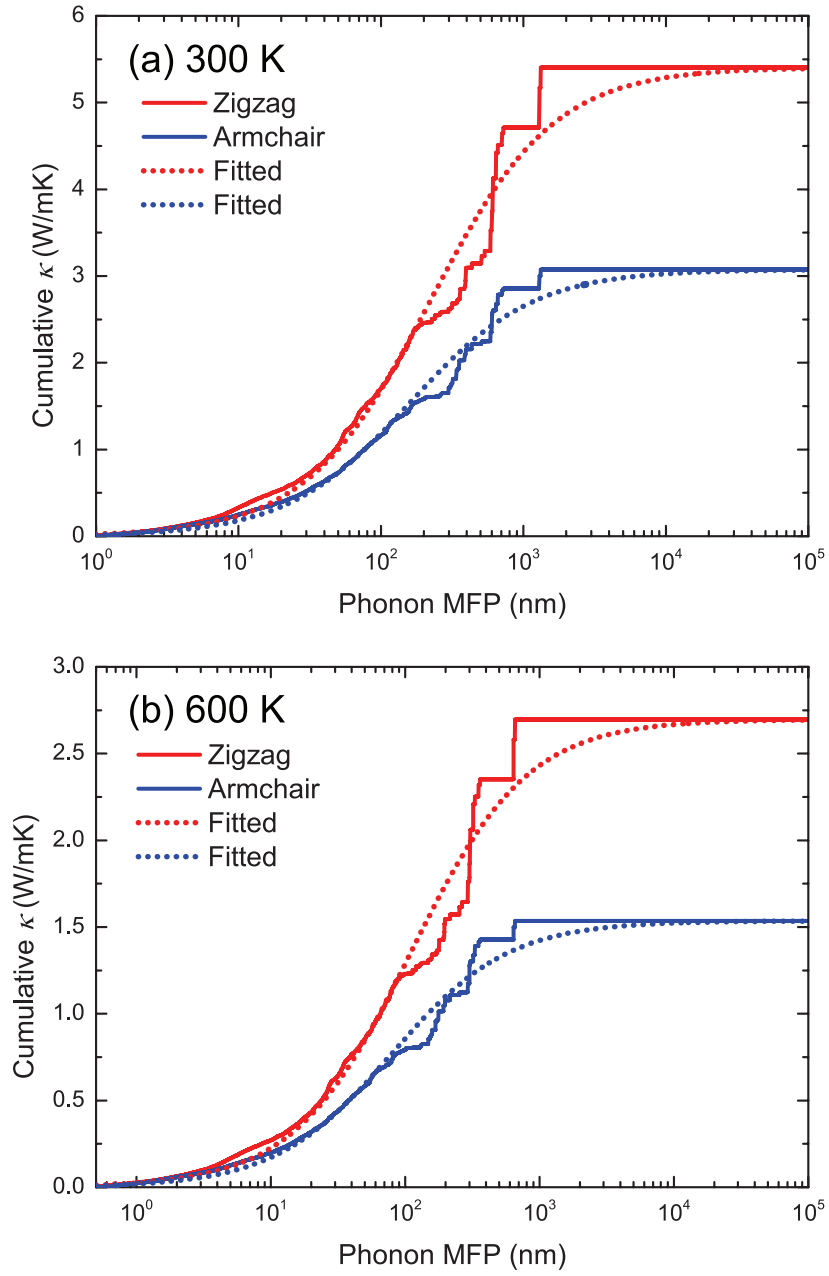


FIG. 8. Cumulative lattice thermal conductivity of stanene along zigzag (red) and armchair (blue) directions as a function of the phonon MFP at (a) 300 K and (b) 600 K. The curves fitted by Eq. (6) are plotted with dot lines.

isotopically pure stanene by solving the phonon Boltzmann transport equation (BTE) using the ShengBTE code<sup>10</sup>, which is completely parameter-free and based only on the information of the chemical structure.

---

\* zhangh@fudan.edu.cn

<sup>1</sup> B. F. Ferrari Andrea C and et. al., *Nanoscale* **7**, 4598 (2015).

<sup>2</sup> K. S. Novoselov, V. I. Fal[prime]ko, L. Colombo, P. R. Gellert, M. G. Schwab, and K. Kim, *Nature* **490**, 192 (2012).

<sup>3</sup> M. Buscema, M. Barkelid, V. Zwiller, H. S. J. van der Zant, G. A. Steele, and A. Castellanos-Gomez, *Nano Letters* **13**, 358 (2013), pMID: 23301811, <http://dx.doi.org/10.1021/nl303321g>.

<sup>4</sup> J. Klinovaja and D. Loss, *Phys. Rev. B* **88**, 075404 (2013).

- <sup>5</sup> F.-f. Zhu, W.-j. Chen, Y. Xu, C.-l. Gao, D.-d. Guan, C.-h. Liu, D. Qian, S.-C. Zhang, and J.-f. Jia, Nat Mater **advance online publication**, (2015).
- <sup>6</sup> Y. Xu, B. Yan, H.-J. Zhang, J. Wang, G. Xu, P. Tang, W. Duan, and S.-C. Zhang, Phys. Rev. Lett. **111**, 136804 (2013).
- <sup>7</sup> Y. Xu, Z. Gan, and S.-C. Zhang, Phys. Rev. Lett. **112**, 226801 (2014).
- <sup>8</sup> G. Qin, Q.-B. Yan, Z. Qin, S.-Y. Yue, H.-J. Cui, Q.-R. Zheng, and G. Su, Sci. Rep. **4**, (2014).
- <sup>9</sup> Z. Fan, J. Zheng, H.-Q. Wang, and J.-C. Zheng, Nanoscale Research Letters **7**, 570 (2012), 10.1186/1556-276X-7-570.
- <sup>10</sup> W. Li, J. Carrete, N. A. Katcho, and N. Mingo, Computer Physics Communications **185**, 1747 (2014).
- <sup>11</sup> A. Jain and A. J. H. McGaughey, Sci. Rep. **5**, 8501 (2015).
- <sup>12</sup> G. Qin, Q.-B. Yan, Z. Qin, S.-Y. Yue, M. Hu, and G. Su, Phys. Chem. Chem. Phys. **17**, 4854 (2015).
- <sup>13</sup> J. Carrete, N. Mingo, and S. Curtarolo, Applied Physics Letters **105**, 101907 (2014).
- <sup>14</sup> S. Cahangirov, M. Topsakal, E. Aktürk, H. Şahin, and S. Ciraci, Phys. Rev. Lett. **102**, 236804 (2009).
- <sup>15</sup> A. H. Castro Neto, F. Guinea, N. M. R. Peres, K. S. Novoselov, and A. K. Geim, Rev. Mod. Phys. **81**, 109 (2009).
- <sup>16</sup> S.-H. Na and C.-H. Park, Journal of the Korean Physical Society **56**, 494 (2010).
- <sup>17</sup> D. L. Nika, E. P. Pokatilov, A. S. Askerov, and A. A. Balandin, Phys. Rev. B **79**, 155413 (2009).
- <sup>18</sup> A. Molina-Sánchez and L. Wirtz, Phys. Rev. B **84**, 155413 (2011).
- <sup>19</sup> X. Gu and R. Yang, Journal of Applied Physics **117**, 025102 (2015).
- <sup>20</sup> C. A. Bryant and P. H. Keesom, Phys. Rev. **123**, 491 (1961).
- <sup>21</sup> Z. L. Yong Xu and W. Duan, Small **10**, 2182 (2014).
- <sup>22</sup> W. Li, J. Carrete, and N. Mingo, Applied Physics Letters **103**, 253103 (2013).
- <sup>23</sup> P. B. Kaul and V. Prakash, Journal of Applied Physics **115**, 023520 (2014).
- <sup>24</sup> J. M. Ziman, *Electrons and Phonons: The Theory of Transport Phenomena in Solids*, edited by E. C. B. N. F. Mott and D. H. Wilkinson (Oxford University Press, 1960).
- <sup>25</sup> G. Grimvall, *Thermophysical properties of materials* (Elsevier Science, 1999).
- <sup>26</sup> L. Lindsay, D. A. Broido, and N. Mingo, Phys. Rev. B **82**, 115427 (2010).
- <sup>27</sup> D. Parker and D. J. Singh, Phys. Rev. B **82**, 035204 (2010).
- <sup>28</sup> J. J. Pulikkotil, D. J. Singh, S. Auluck, M. Saravanan, D. K. Misra, A. Dhar, and R. C. Budhani, Phys. Rev. B **86**, 155204 (2012).
- <sup>29</sup> H. Xie, M. Hu, and H. Bao, Applied Physics Letters **104**, 131906 (2014).
- <sup>30</sup> J. Liu, G.-M. Choi, and D. G. Cahill, Journal of Applied Physics **116**, 233107 (2014).
- <sup>31</sup> X. Li, J. T. Mullen, Z. Jin, K. M. Borysenko, M. Buongiorno Nardelli, and K. W. Kim, Phys. Rev. B **87**, 115418 (2013).
- <sup>32</sup> Y. Cai, J. Lan, G. Zhang, and Y.-W. Zhang, Phys. Rev. B **89**, 035438 (2014).
- <sup>33</sup> Z.-Y. Ong and E. Pop, Phys. Rev. B **84**, 075471 (2011).
- <sup>34</sup> A. Pisoni, J. Jacimovic, O. S. Bari, A. Walter, B. Nfrdi, P. Bugnon, A. Magrez, H. Berger, Z. Revay, and L. Forr, The Journal of Physical Chemistry C **119**, 3918 (2015), <http://dx.doi.org/10.1021/jp512013n>.
- <sup>35</sup> D. K. Efetov and P. Kim, Phys. Rev. Lett. **105**, 256805 (2010).
- <sup>36</sup> J. Ziman, Scientific American **217** (1967).
- <sup>37</sup> L. Lindsay, W. Li, J. Carrete, N. Mingo, D. A. Broido, and T. L. Reinecke, Phys. Rev. B **89**, 155426 (2014).
- <sup>38</sup> X. Gu and R. Yang, Applied Physics Letters **105**, 131903 (2014).
- <sup>39</sup> L. Lindsay and D. A. Broido, Journal of Physics: Condensed Matter **20**, 165209 (2008).
- <sup>40</sup> G. Kresse and J. Furthmüller, Phys. Rev. B **54**, 11169 (1996).
- <sup>41</sup> S. Baroni, S. de Gironcoli, A. Dal Corso, and P. Giannozzi, Rev. Mod. Phys. **73**, 515 (2001).
- <sup>42</sup> A. Togo, F. Oba, and I. Tanaka, Phys. Rev. B **78**, 134106 (2008).